

# Phase-manipulation-induced Majorana Mode and Braiding Realization in Iron-based Superconductor Fe(Te,Se)

Rui Song,<sup>1, 2, 3, 4</sup> Ping Zhang,<sup>5, 2, 4, 6</sup> and Ning Hao<sup>3, \*</sup>

<sup>1</sup>HEDPS, Center for Applied Physics and Technology and School of Physics, Peking University, Beijing 100871, China

<sup>2</sup>HEDPS, Center for Applied Physics and Technology and School of Engineering, Peking University, Beijing 100871, China

<sup>3</sup>Anhui Key Laboratory of Condensed Matter Physics at Extreme Conditions,  
High Magnetic Field Laboratory, HFIPS, Anhui,

Chinese Academy of Sciences, Hefei, 230031, China

<sup>4</sup>Institute of Applied Physics and Computational Mathematics, Beijing 100088, China

<sup>5</sup>School of Physics and Physical Engineering, Qufu Normal University, Qufu 273165, China

<sup>6</sup>Beijing Computational Science Research Center, Beijing 100084, China

Recent experiment reported the evidence of dispersing one-dimensional Majorana mode trapped by the crystalline domain walls in FeSe<sub>0.45</sub>Te<sub>0.55</sub>. Here, we perform the first-principles calculations to show that iron atoms in the domain wall spontaneously form the ferromagnetic order in line with orientation of the wall. The ferromagnetism can impose a  $\pi$  phase difference between the domain-wall-separated surface superconducting regimes under the appropriate width and magnetization of the wall. Accordingly, the topological surface superconducting state of FeSe<sub>0.45</sub>Te<sub>0.55</sub> can give rise to one-dimensional Majorana modes bounded by the wall. More importantly, we further propose a surface phase battery junction in the form of FeSe<sub>0.45</sub>Te<sub>0.55</sub>/ferromagnet/FeSe<sub>0.45</sub>Te<sub>0.55</sub>, which can be adopted to create and fuse the Majorana zero modes through controlling the width or magnetization of the interior ferromagnetic barrier. The braiding and readout of Majorana zero modes can be realized by the designed device. Such surface phase battery junction has the potential application in the superconducting topological quantum computation.

Majorana zero modes (MZMs) have attracted intense attention in condensed matter physics for the possible application in topological quantum computation[1–6]. The paradigm for persuing them is due to inducing pairing of electrons to the spin-momentum-locked bands by means of superconducting proximity effect in the artificial solid-state physical systems. The candidate platforms mainly includes the topological insulator, the Rashba-spin-orbit-coupled semiconductor and the ferromagnetic atomic chains forming the heterostructures with the conventional s-wave superconductors [7–11]. However, the weakness of the induced superconductivity from the proximity effect requires the ultra-low temperature condition and limits the potential applications in these systems.

Recently, the electronic bands with nontrivial topological features have been theoretically predicted and experimentally verified in some iron-based superconductors[12–17]. The coexistence of topological bands and high-temperature superconductivity make the iron-based superconductors as the unique platform to realize the high-temperature topological superconductors[15, 18–21]. Besides, some theoretical proposals further discussed the possibility to realize the high-order topological superconductivity by these iron-based superconductors[22–26]. In general, some kinds of defects can bound the MZMs in topological superconductors. Assisted by angle resolved photoelectron spectroscopy (ARPES), the scanning tunnel microscope/spectrum (STM/S) has observed the zero-energy conductance anomalies located on some point defect such as iron impurity and superconducting vortex in Fe(Se,Te), Li<sub>1-x</sub>Fe<sub>x</sub>HOFeSe, CaKFe<sub>4</sub>As<sub>4</sub>,

and Fe(Se,Te)/STO which strongly indicate the emergence of MZMs[27–32]. Unlike the point-like MZMs, more recently, an unexpected one-dimensional (1D) dispersive Majorana mode bounded by the crystalline domain walls (DWs) in FeSe<sub>0.45</sub>Te<sub>0.55</sub> have been experimentally reported[33]. It is found that the DWs and 1D Majorana mode show some interesting features. For instance, the lattices form the bulge structure approaching the DWs. The orientation of the DW has a deflection of about a 45 degree angle against the direction of lattice shift. The differential conductance  $dI/dV$  spectra show some subtle differences at the different positions of DWs. However, the physical origin and the features of the 1D Majorana mode have not been comprehensively understood.

In this work, we perform the first-principles calculations to investigate the properties of the DWs in FeSe<sub>0.45</sub>Te<sub>0.55</sub>. The numerical results can capture both the bulge structure and the specific orientation of the DWs. Interestingly, we find that the iron atoms in the DWs spontaneously form the ferromagnetic order with the magnetization direction along the DWs. Accordingly, we show that the ferromagnetism can manipulate the surface superconducting phase difference between the two sides of the DWs, which is analogous to the physical picture of Fulde-Ferrell-Larkin-Ovchinnikov (FFLO) superconducting state[34, 35]. The appropriate width and magnetization of the DWs can give  $\pi$  phase difference and induce 1D Majorana mode. The fluctuations of the width and magnetization of the DWs make the phase difference to slightly deviate from  $\pi$ , which results in the subtle differences of  $dI/dV$  spectra at the

different positions of DWs. More importantly, we further propose a surface phase battery junction in the form of  $\text{FeSe}_{0.45}\text{Te}_{0.55}$ /ferromagnet/ $\text{FeSe}_{0.45}\text{Te}_{0.55}$ . Tuning the width or magnetization in the different regimes of the ferromagnet, the surface phase battery junction can be adopted to create and fuse the MZMs located on the boundary between different regimes. The braiding and readout of MZMs can be realized by the designed device based on such junction.

As the STM experiment shows, the DWs are a line of dislocation-like defects, which separate the lattices into left and right parts with a relative half-unit-cell shift[33]. The thickness of DWs is one or several unit cells of  $\text{Fe}(\text{Te},\text{Se})$  from experimental observation[36]. Therefore, we construct a  $14 \times 1 \times 1$  supercell of  $\text{Fe}(\text{Te},\text{Se})$ , and the left and right seven unit cells are connected by a horizontal mirror reflection about iron plane. The calculation details are present in supplementary materials (SMs). After dynamic-relaxation, the energy- and force-converged structure is displayed in Fig. 1 (a)-(c), which shows a obvious bulge structure deformation. The simulated STM image in Fig. 1 (d) reveals that the DWs are much lighter than other regions in accord with the experimental observations (See Sec. I in SMs for details). Furthermore, the deflection of about a 45 degree angle of the orientation of the DW against the direction of half-unit-cell shift is also captured by the simulation in comparison with image in Fig. 3(d) of Ref.[33]. The bulge structure deformation is due to the unsymmetric Fe-Te(Se) chemical bonds in the DWs, which break the force balance along  $z$  direction. The unsymmetric Fe-Te(Se) chemical bonds have another impact to enhance the localization of iron atoms in the DWs, which have a tendency to generate the magnetic moments. To determine the possible magnetic order of the DWs, for convenience, we still assume the  $\text{Fe}(\text{Te},\text{Se})$  at the two sides of DWs possess the antiferromagnetic (AFM) order in spite of only strong AFM fluctuation existing in  $\text{Fe}(\text{Se},\text{Te})$ . This is the general strategy adopted by the calculations to determine the magnetism of iron-based superconductors[37–39]. It is well accepted that the superconducting state in  $\text{Fe}(\text{Te},\text{Se})$  has a close relationship with the collinear AFM order. Thus, we consider the  $\text{Fe}(\text{Te},\text{Se})$  at the two sides of DWs have the such collinear AFM order, as shown in Fig. 1 (a) and (b). For the iron atoms in the DWs, we consider the AFM and FM pattern in Fig. 1 (a) and (b), respectively. The ground-state magnetic pattern is self-consistently determined by calculating the energy. As shown in Fig. 1 (e), the magnetic pattern in Fig. 1 (b) has lower energy than that in Fig. 1 (a). The Hubbard  $U$  can further enlarge the energy difference. The calculated results are not unexpected, because the position switchings of the anions do not dramatically modulate the amplitudes of the nearest and next nearest neighbor exchange couplings. According to the  $J_1$ - $J_2$  model[39–41], the magnetic pattern shown in Fig. 1 (b) is reasonable. Note that we also

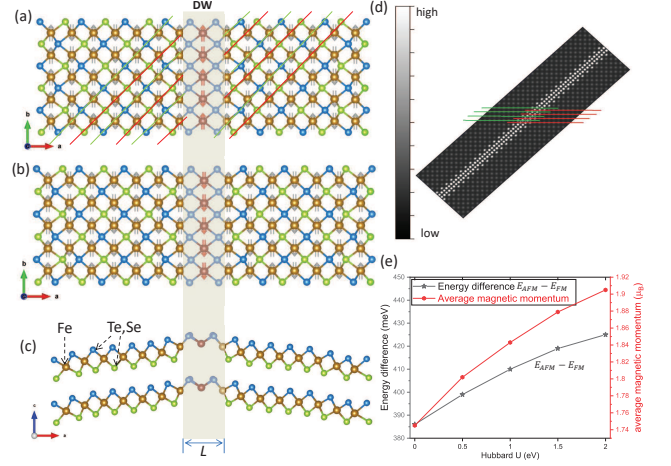


FIG. 1: (a)-(c) Top and side view of  $\text{Fe}(\text{Te},\text{Se})$  with  $14 \times 1 \times 1$  super cell with DW labeled by the shadowed region. In both (a) and (b), the two sides of the DW have the collinear AFM order, but the iron atoms have the AFM and FM order in the DW in (a) and (b), respectively. (c) The simulated STM pattern. (d) The magnetic momentum and the energy difference between the magnetic patterns in (a) and (b), i.e.,  $E_{AFM} - E_{FM}$ .

calculate the lattice pattern with domain walls involving two lines of irons. The same ferromagnetic order is also obtained (See Sec. I in SMs for details).

When the temperature drops below the superconducting transition temperature  $T_c$ , the superconductivity arises through suppressing the collinear AFM order or spin fluctuation in normal regimes, while the FM order in the DWs is preserved due to the absence of superconductivity. Then, the system can be simplified as a surface superconductor/ferromagnet/superconductor (S/F/S) junction which only involving the topological surface states, as shown in Fig. 2(a). The ferromagnetism of the DWs could generate an exchange field, which can be considered as an effective Zeeman field, i.e.,  $h_y = (n \langle S_i^y \rangle / \mu_B) \int J(\mathbf{r}) d^3r$ , with  $n$ ,  $S_i^y$ ,  $\mu_B$ , and  $J(\mathbf{r})$  labeling the concentration of localized moments, the average value of the localized spins, Bohr magneton and ferromagnetic exchange integral, respectively. Hereafter, we set  $\mu_B = 1$  for convenience. Back to the surface S/F/S junction, it is shown that the F layer can generally modulate a superconducting phase difference between the two S layers. Here, we give a simple picture to address this point. Consider the normal Fermi surface of both S layer described by the topological surface Hamiltonian  $H_{surf} = v_F(\sigma \times \mathbf{k}) \cdot \hat{z}$ , the Fermi surface of the right S layer is shifted  $\mathbf{Q} = h_y / v_F \hat{\mathbf{k}}_x$  by the effective Zeeman term  $g \sigma_y h_y / 2$  in reference to the one of the left S layer. From the first-principles calculations, we can estimate the effective Zeeman energy  $h_y \sim 55$  meV (See Sec. I in SMs for details). The Fermi velocity  $v_F \sim 216$  meV  $\text{\AA}$

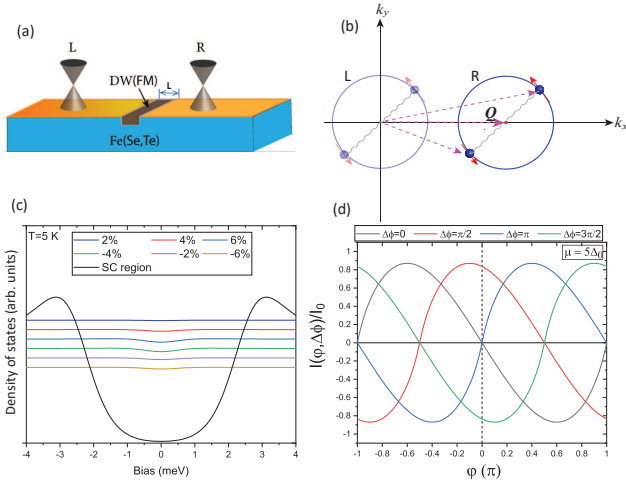


FIG. 2: (a) Schematic plotting for the surface S/F/S junction. The left (L) and right (R) gray Dirac cones denote the topological surface bands of Fe(Te,Se), and the middle labels the ferromagnetic DW. (b) The Fermi surface of the R Dirac cone shifts momentum  $Q$  in the reference of L Dirac cone. The pairing is indicated by the wave lines. (c) The calculated density of states (DOS) for the different  $\Delta\phi$  fluctuations [-6%, 6%] about  $\pi$ . The U-shape DOS is for the uniform superconducting state. The temperature is 5K. (d) The oscillation of tunneling current  $I(\phi, \Delta\phi)$  about  $\varphi$  for different  $\Delta\phi$ . Note that the current is not zero for  $\varphi = 0$  and  $\Delta\phi \neq 0, \pi$ , which is different from the conventional junction.

and  $k_F \sim 0.03 \text{\AA}^{-1}$  [42]. Thus  $Q \sim 0.25 \text{\AA}^{-1}$ , and  $Q \gg k_F$ . The left and right Fermi surfaces are fully separated, as shown in Fig. 2(b). In the superconducting state, the s-wave singlet pairing potential requests two electrons with opposite spin pairing with each other. Under the mean-field approximation, the superconducting order parameter  $\Delta(\mathbf{Q})$  is proportional to  $\langle \hat{c}_{\mathbf{k}\uparrow} \hat{c}_{2\mathbf{Q}-\mathbf{k}\downarrow} \rangle$ , which becomes spatially oscillating after Fourier transform into the real space. Namely,  $\Delta(\mathbf{R}) = \Delta_0 e^{i2\mathbf{Q} \cdot \mathbf{R}}$  with  $\Delta_0$ ,  $\mathbf{R}$  labeling the induced superconducting order parameter of the topological surface band and the coordinate of center of mass of Cooper pair, respectively. This is equivalent to stating that a Cooper pair propagates across a Zeeman field and acquire a finite momentum and a phase oscillation in the real space, which is similar to the FFLO state [34, 35]. The phase shift is related to the width  $L$  and intensity of the effective Zeeman field  $h_y$  of DWs and can be expressed as  $\Delta\phi = 2h_y L / v_F$ . When the system is in equilibrium state, no random phase difference occurs between the left and right superconducting regions, however, the system becomes a surface  $\Delta\phi$ -junction due to the phase-shift effect. According to Fu and Kane's theorem [7], a 1D Majorana model will arise in the DWs when  $\Delta\phi = \pi$  in the limit of  $L$  approaching zero.

To verify the argument, we consider the generic surface S/F/S junction with arbitrary width  $L$  and effective Zee-

man field  $h_y$  of DWs, and solve the Dirac-Bogoliubov-de Gennes (BdG) equation,

$$H_{BdG} \Psi = E \Psi, \quad (1)$$

with

$$H_{BdG} = \begin{pmatrix} H_0(k) & i\sigma_y \Delta(r) \\ -i\sigma_y \Delta^*(r) & -H_0^*(-k) \end{pmatrix}. \quad (2)$$

Here,  $H_0(k) = v_F(\sigma_x k_y - \sigma_y k_x) - \mu + \sigma_y h_y \Theta(\frac{L}{2} - |x|)$  and  $\Delta(r) = \Delta_0 e^{-i\frac{\varphi}{2}} \Theta(-x - \frac{L}{2}) + \Delta_0 e^{i\frac{\varphi}{2}} \Theta(x - \frac{L}{2})$ , and  $\Theta$  is the Heaviside step function,  $\varphi$  is the assumed random phase difference between two surface superconducting regimes. The details of the analytic calculation of the Dirac-BdG equation in Eq. (1) are shown in Sec. II in SMs. Here, we only discuss the main results. For both  $\mu \rightarrow 0$  and  $\mu \gg \Delta_0$ , two branches of bound states for the two cases have the same dispersion,

$$\varepsilon(k_y) = \pm \sqrt{v_F^2 k_y^2 + \Delta_0^2 \cos^2(\frac{\varphi}{2} - \frac{h_y L}{v_F})}. \quad (3)$$

Here,  $k_y \rightarrow 0$  for  $\mu \rightarrow 0$ , and  $k_y = \mu / v_F \sin \theta$  with  $\theta$  the incident angle approaching 0. In equilibrium state, the initial random phase difference  $\varphi = 0$ , however, a couple of gapless bound states can still obtained when  $\frac{h_y L}{v_F} = \frac{\Delta\phi}{2} = \frac{\pi}{2}$ . Namely, 1D dispersive Majorana modes with constant density of states (DOS) are realized for the FM DWs with appropriate width  $L$  and magnetization characterized by  $h_y$ . For finite  $\mu$ , the effective low-energy Hamiltonian describing a couple of bound states can be obtained by projecting  $H_{BdG}$  into the subspace spanned by two eigenstates  $\xi_{\pm}$  corresponding to  $\varepsilon(k_y) = 0$  with  $k_y = 0$ ,  $\varphi = 0$  and  $\frac{h_y L}{v_F} = \frac{\pi}{2}$  [7]. Here,  $\xi_{\pm} = \frac{1}{2}(\mp i, -1, \pm i, 1)^T e^{\pm i\mu x / v_F - \int_0^{|x|} d\tilde{x} \Delta_0(\tilde{x}) / v_F}$ . Then, the effective low-energy Hamiltonian has the form,

$$H_{eff} = \tilde{v}_F q_y \tau_y - \Delta_0 \cos(\Delta\phi/2) \tau_z. \quad (4)$$

Here,  $\tilde{v}_F = v_F [\cos k_F L + (\Delta_0 / \mu) \sin k_F L] \Delta_0^2 / (\mu^2 + \Delta_0^2)$ .  $\tau_y$  and  $\tau_z$  are Pauli matrices spanned by particle-hole space. When  $\Delta\phi = \pi$ ,  $H_{eff}$  in Eq. (4) also gives the 1D dispersive Majorana modes with constant DOS.

The implication for the experimental observations [33] can be elucidated as follows. The calculated effective Zeeman energy  $h_y \sim 55$  meV. The width of DW is about twice about the lattice constant  $L \sim 6.2$  Å. The Fermi velocity  $v_F \sim 216$  meVÅ [42]. Thus the phase shift can be derived as  $\Delta\phi \sim \pi$ , which indicates that the 1D dispersive Majorana modes in Fe(Te,Se) is likely to be induced due to the ferromagnetism of DWs. However, the realistic sample could not meet such rigorous condition of  $\Delta\phi = \pi$ . There should exist some slight fluctuations of  $h_y$  and  $L$  in the sample. Accordingly,  $\Delta\phi$  should have tiny fluctuations around  $\pi$ . As a result, the experiment

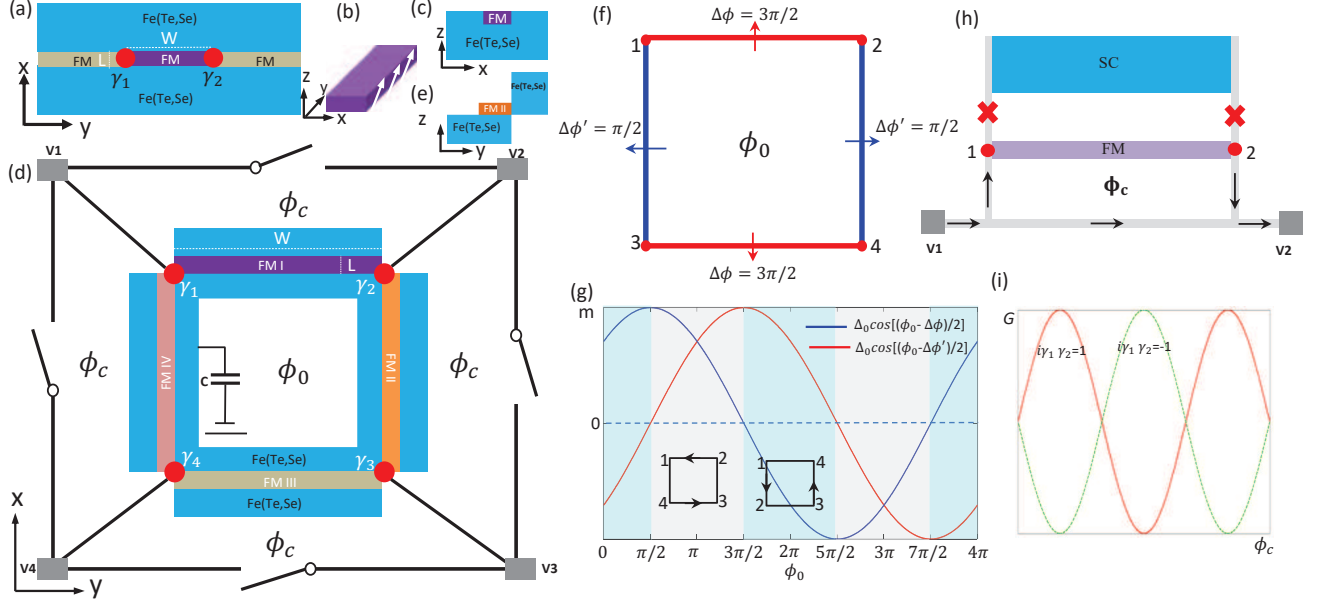


FIG. 3: (a) A basic device which can create and fuse a pair of MZMs through tuning the magnetization of different regimes of the FM film. (b) The magnetic moments (white arrows) of the FM film can be tuned in the  $y$ - $z$  plane by some external field. (c) The cross section of the middle part in (a). (d) The extended device built from the basic device. There are four FM films labeled by I, II, III, IV. Tuning the corresponding magnetization can realize two pairs of corner MZMs.  $\phi_0$  denotes the magnetic flux through the superconducting loop. The superconductor is connected to ground by a capacitor. A braiding operation is finished when  $\phi_0$  adiabatically advances from 0 to  $2\pi$ . During the braiding process, the four switches are disconnected. To readout the braiding result of arbitrary pair of MZMs, the corresponding switch is connected to form the interference circuit, as shown in (h). The magnetic flux  $\phi_c$  is adopted to detect the fermion parity  $i\gamma_j\gamma_{j+1}$ , as shown in (i). (e) The cross section of left edge of the square in (d). (f) The square denotes the loop formed by the four FM films.  $\Delta\phi = 3\pi/2$  and  $\Delta\phi' = \pi/2$  denote the values of  $2h_y L/v_F$  in regime I, III and II, IV, respectively. (g) The evolution of two masses  $m^{(n)} = \Delta_0 \cos[(\phi_0 - \Delta\phi^{(n)})/2]$  as magnetic flux  $\phi_0$ . The insert labels the equivalent exchange process of MZMs during the braiding. (h) The equivalent interference circuit to readout fermion parity of  $i\gamma_1\gamma_2$ . Note that the superconductor path is disconnected by the capacitor in (d). (i) The interference oscillation of conductance as change as  $\phi_c$  for different fermion parity.

indeed observed the differential conductance  $dI/dV$  spectra showed some subtle differences at the different positions of DWs[33]. Such behavior is captured by the calculation, as shown in Fig. 2 (c). Besides, the picture of such surface S/F/S junction proposed here can also be verified by measure the tunneling current, which can be expressed as,

$$I(\varphi, \Delta\phi) = -\frac{eN}{\hbar} \int_{-\pi/2}^{\pi/2} \frac{\partial|\varepsilon(k_y)|}{\partial\varphi} \tanh \frac{|\varepsilon(k_y)|}{2k_B T} \cos\theta d\theta. \quad (5)$$

Here,  $k_B$  is Boltzmann constant.  $N = k_F W/\pi$  denoting the number of the transport channels in the system with  $W$  the length of the domain wall.  $k_y = k_F \sin\theta$  with  $\theta$  labeling the incident angle. As shown in Fig. 2 (d), the tunneling current  $I(\varphi, \Delta\phi)$  is none zero for  $\varphi = 0$  and  $\Delta\phi \neq 0$  and  $\pi$ . Thus, the surface states of  $\text{FeSe}_{0.45}\text{Te}_{0.55}$  with domain wall form a  $\Delta\phi$  phase battery[43].

According to the effective low-energy Hamiltonian in Eq. (4), the boundary of the inverse masses can trap a MZM[7]. Thus, the aforementioned surface S/F/S junction

can be upgraded by replacing the DWs with a thin FM film. According to  $\Delta\phi = 2h_y L/v_F$ , there are two ways to realize MZMs. The first one is to tune  $h_y$  of different regimes of F. In such case, the FM film can be fabricated with the soft magnetic materials, whose magnetization can be easily tuned by the electric, magnetic field etc., as shown in Fig. 3 (b). The second one is to tune  $L$  of different regimes of F, where the hard magnetic materials can be adopted to fabricate the FM film due to the robust magnetization. In both cases, the candidate magnetic materials could be selected among the yttrium iron garnet (YIG) ferrite, which includes many soft and hard ferrites such as  $(\text{MnZn})\text{O} \cdot \text{Fe}_2\text{O}_3$  and  $\text{BaO} \cdot 6\text{Fe}_2\text{O}_3$ , and the relevant film technique is very mature. Here, we adopt the first way, and the basic device is shown in Fig. 3 (a) and (c). The different colors in the F denotes the different  $h_y$  and relevant different mass  $m(h_y) = \Delta_0 \cos(h_y L/v_F)$ . Tune  $h_y$  to have  $m(h_y) < 0$  in the middle regime of F and  $m(h_y) > 0$  in two side regimes, a pair of MZMs can be created at the boundaries of middle and side regimes. They can also fuse



by adiabatically tuning  $m(h_y)$  to have same sign in all regimes. Namely, such basic device can realize the creation and fusion of a pair of MZMs through selectively tuning the magnetization  $h_y$  of F.

To braid the MZMs[44–52] and make the braiding results detectable, the basic device has to be extended to have two pairs of MZMs at least. The new device is shown in Fig. 3 (d) and (e). Note that the cross section has to be designed as the configuration in Fig. 3 (e), because the superconducting square in Fig. 3 (e) has to be disconnected with the outer superconductors to induce the phase different by the magnetic flux  $\phi_0$ . The thin enough FM films guarantee the applicability of the above surface S/F/S model. First, we tune the  $h_y$  to have  $m(h_y) < 0$  in I, III regimes and  $m(h_y) > 0$  in II, IV regimes. The configuration is shown in Fig. 3 (f). Two pairs of MZMs labeled by  $\gamma_1, \gamma_2, \gamma_3, \gamma_4$  are created and located on the four corners of the square. Now, two fermions can be defined as  $f_1 = (\gamma_1 + i\gamma_2)/2$  and  $f_2 = (\gamma_3 + i\gamma_4)/2$ . Suppose the initial state is occupied state of the two fermions, *i.e.*,  $|11\rangle = f_1^\dagger f_2^\dagger |00\rangle$  with  $|00\rangle$  the vacuum state of both fermions. Second, the braiding operation is realized by adiabatically advancing the phase of inner superconductor square loop from 0 to  $2\pi$ . During the process, the mass term  $m = \Delta_0 \cos[(\phi_0 - \Delta\phi)/2]$  also adiabatically evolves, as shown in Fig. 3 (e). This braiding operation is equivalent to exchange  $\gamma_2$  and  $\gamma_4$ , *i.e.*,  $\gamma_2 \rightarrow \gamma_4, \gamma_4 \rightarrow -\gamma_2$ , as shown in the insert of Fig. 3 (g). Here, we assume the cut line is the right edge of the square[7]. The relevant braiding operator is  $\mathcal{O}_{42} = (1 + \gamma_4\gamma_2)/\sqrt{2}$ , under which, the final state  $|\Psi_f\rangle_1 = \mathcal{O}_{42}|11\rangle = (|11\rangle - |00\rangle)/\sqrt{2}$ . The twice braidings give  $|\Psi_f\rangle_2 = \mathcal{O}_{42}^2|11\rangle = -|00\rangle$ , which means the fermion occupied number changes two. Note that the braiding result is same to exchange  $\gamma_1$  and  $\gamma_3$  and pin  $\gamma_2$  and  $\gamma_4$ . Third, the braiding results can be readout by electron teleportation effect of MZMs[44, 45]. The constructed interference circuit is shown in Fig. 3 (d). Take a pair of  $\gamma_1, \gamma_2$  as an example. To detect the braiding results of fermion parity of  $i\gamma_1\gamma_2$ , one can connect the switch between  $v_1$  and  $v_2$  in Fig. 3 (d) and apply a magnetic flux  $\phi_c$ . The equivalent circuit is shown in Fig. 3 (h). The current flows along two different paths indicated by the arrows in Fig. 3 (h). Note that the superconductor path can be forbidden by tuning the capacitor in Fig. 3 (d). Accordingly, the measured conductance should form interference oscillation as change as  $\phi_c$ , *i.e.*,  $G = g_0 + i\gamma_1\gamma_2g_1 \cos[e(\phi_c - \phi_i)/\hbar]$  with  $\phi_i$  the intrinsic phase difference[45], and the fermion parity of  $i\gamma_1\gamma_2$  can be readout, as shown in Fig. 3 (i)[44, 45]. The twice braiding can give the result of definitive sign change of  $i\gamma_1\gamma_2$  between the initial and final states.

At last, we discuss the experimental feasibility and advantage of the designed device. First, the decay length of MZM is  $\xi_0 \sim \tilde{v}_F/\Delta_0 \sim 7\text{\AA}$  for  $\mu = 5\Delta_0$ ,  $v_F \sim 216\text{ meV\AA}$  and  $\Delta_0 \sim 1.8\text{ meV}$ [21, 33, 42]. The size of MZM is very local. Second, the other quasi-particle energy is

roughly estimated by  $\sim \tilde{v}_F\pi/W$ [7]. If the temperature  $k_B T \sim 0.1\text{ meV\AA}$ . The length of  $W$  in Fig. 3 (d) can be  $\sim 27\text{ nm}$  for  $\mu = 5\Delta_0$ , which is much larger than the decay length  $\xi_0$ . When temperature is below 1 K  $\sim 0.1\text{ meV}$ , the MZMs and relevant braiding are robust against the thermal fluctuation. The charging energy  $U \sim Q_0^2/C$  is required to comparable to  $\Delta_0 \sim 1.8\text{ meV}$ [44, 45], which can lower the difficulty in control of the capacitor.

In conclusion, we propose a surface S/F/S junction to reveal the underlying physics of experimentally observed dispersive one-dimensional Majorana mode in  $\text{FeSe}_{0.45}\text{Te}_{0.55}$ . Our calculations predict the spontaneously ferromagnetic order in the domain wall, and we prove the crucial role of ferromagnetism to modulate the superconducting phase of the surface electrons to form Majorana modes. More importantly, we design a feasible artificial device involving  $\text{FeSe}_{0.45}\text{Te}_{0.55}$ /ferromagnet/ $\text{FeSe}_{0.45}\text{Te}_{0.55}$  junctions, which can easily create, fuse, braid and readout the Majorana zero modes.

We thank J. P. Hu, X. X. Wu, S. B. Zhang, S. S. Qin, F. W. Zheng, H. F. Du, L. Shan, Z. Y. Wang, S. C. Yan and X. Y. Hou for helpful discussions. This work was financially supported by the National Key R&D Program of China No. 2017YFA0303201, National Natural Science Foundation of China under Grants (No. 12022413, No. 11674331, No.11625415), the ‘‘Strategic Priority Research Program (B)’’ of the Chinese Academy of Sciences, Grant No. XDB33030100, the ‘100 Talents Project’ of the Chinese Academy of Sciences, the Collaborative Innovation Program of Hefei Science Center, CAS (Grants No. 2020HSC-CIP002), the CASHIPS Director’s Fund (BJPY2019B03), the Science Challenge Project under Grant No. TZ2016001. A portion of this work was supported by the High Magnetic Field Laboratory of Anhui Province, China.

---

\* Electronic address: haon@hmf.ac.cn

- [1] D. A. Ivanov, Phys. Rev. Lett. **86**, 268 (2001).
- [2] A. Y. Kitaev, Ann. Phys. **303**, 2 (2003).
- [3] A. Kitaev, Ann. Phys. **321**, 2 (2006).
- [4] C. Nayak, S. H. Simon, A. Stern, M. Freedman, and S. Das Sarma, Rev. Mod. Phys. **80**, 1083 (2008).
- [5] J. Alicea, Rep. Prog. Phys. **75**, 076501 (2012).
- [6] S. R. Elliott and M. Franz, Rev. Mod. Phys. **87**, 137 (2015).
- [7] L. Fu and C. L. Kane, Phys. Rev. Lett. **100**, 096407 (2008).
- [8] J. D. Sau, R. M. Lutchyn, S. Tewari, and S. Das Sarma, Phys. Rev. Lett. **104**, 040502 (2010).
- [9] R. M. Lutchyn, J. D. Sau, and S. Das Sarma, Phys. Rev. Lett. **105**, 077001 (2010).
- [10] Y. Oreg, G. Refael, and F. von Oppen, Phys. Rev. Lett. **105**, 177002 (2010).
- [11] S. Nadj-Perge, I. K. Drozdov, J. Li, H. Chen, S. Jeon, J.

- Seo, A. H. MacDonald, B. A. Bernevig, and A. Yazdani, *Science* **346**, 602 (2014).
- [12] N. Hao and J. Hu, *Phys. Rev. X* **4**, 031053 (2014).
- [13] Z. Wang, P. Zhang, G. Xu, L. K. Zeng, H. Miao, X. Xu, T. Qian, H. Weng, P. Richard, A. V. Fedorov, H. Ding, X. Dai, and Z. Fang, *Phys. Rev. B* **92**, 115119 (2015).
- [14] X. Wu, S. Qin, Y. Liang, H. Fan, and J. Hu, *Phys. Rev. B* **93**, 115129 (2016).
- [15] N. Hao and J. Hu, *Natl. Sci. Rev.* **6**, 213 (2019).
- [16] X. L. Peng, Y. Li, X. X. Wu, H. B. Deng, X. Shi, W. H. Fan, M. Li, Y. B. Huang, T. Qian, P. Richard, J. P. Hu, S. H. Pan, H. Q. Mao, Y. J. Sun, and H. Ding, *Phys. Rev. B* **100**, 155134 (2019).
- [17] P. Zhang, Z. Wang, X. Wu, K. Yaji, Y. Ishida, Y. Kohama, G. Dai, Y. Sun, C. Bareille, K. Kuroda, T. Kondo, K. Okazaki, K. Kindo, X. Wang, C. Jin, J. Hu, R. Thomale, K. Sumida, S. Wu, K. Miyamoto, T. Okuda, H. Ding, G. D. Gu, T. Tamegai, T. Kawakami, M. Sato, and S. Shin, *Nat. Phys.* **15**, 41 (2019).
- [18] X. Wu, S. Qin, Y. Liang, C. Le, H. Fan, and J. Hu, *Phys. Rev. B* **91**, 081111(R) (2015).
- [19] G. Xu, B. Lian, P. Tang, X.-L. Qi, and S.-C. Zhang, *Phys. Rev. Lett.* **117**, 047001 (2016).
- [20] X. Shi, Z.-Q. Han, P. Richard, X.-X. Wu, X.-L. Peng, T. Qian, S.-C. Wang, J.-P. Hu, Y.-J. Sun, and H. Ding, *Sci. Bull.* **62**, 503 (2017).
- [21] P. Zhang, K. Yaji, T. Hashimoto, Y. Ota, T. Kondo, K. Okazaki, Z. Wang, J. Wen, G. D. Gu, H. Ding, and S. Shin, *Science* **360**, 182 (2018).
- [22] Q. Wang, C.-C. Liu, Y.-M. Lu, and F. Zhang, *Phys. Rev. Lett.* **121**, 186801 (2018).
- [23] Z. Yan, F. Song, and Z. Wang, *Phys. Rev. Lett.* **121**, 096803 (2018).
- [24] R.-X. Zhang, W. S. Cole, and S. Das Sarma, *Phys. Rev. Lett.* **122**, 187001 (2019).
- [25] X. Wu, X. Liu, R. Thomale, and C.-X. Liu, *Natl. Sci. Rev.* nwab087 (2021).
- [26] R.-X. Zhang, W. S. Cole, X. Wu, and S. Das Sarma, *Phys. Rev. Lett.* **123**, 167001 (2019).
- [27] J. X. Yin, Z. Wu, J. H. Wang, Z. Y. Ye, J. Gong, X. Y. Hou, L. Shan, A. Li, X. J. Liang, X. X. Wu, J. Li, C. S. Ting, Z. Q. Wang, J. P. Hu, P. H. Hor, H. Ding, and S. H. Pan, *Nat. Phys.* **11**, 543 (2015).
- [28] D. Wang, L. Kong, P. Fan, H. Chen, S. Zhu, W. Liu, L. Cao, Y. Sun, S. Du, J. Schneeloch, R. Zhong, G. Gu, L. Fu, H. Ding, and H.-J. Gao, *Science* **362**, 333 (2018).
- [29] Q. Liu, C. Chen, T. Zhang, R. Peng, Y.-J. Yan, C.-H.-P. Wen, X. Lou, Y.-L. Huang, J.-P. Tian, X.-L. Dong, G.-W. Wang, W.-C. Bao, Q.-H. Wang, Z.-P. Yin, Z.-X. Zhao, and D.-L. Feng, *Phys. Rev. X* **8**, 041056 (2018).
- [30] T. Machida, Y. Sun, S. Pyon, S. Takeda, Y. Kohsaka, T. Hanaguri, T. Sasagawa, and T. Tamegai, *Nat. Mater.* **18**, 811 (2019).
- [31] W. Liu, L. Cao, S. Zhu, L. Kong, G. Wang, M. Papaj, P. Zhang, Y.-B. Liu, H. Chen, G. Li, F. Yang, T. Kondo, S. Du, G.-H. Cao, S. Shin, L. Fu, Z. Yin, H.-J. Gao and H. Ding, *Nat. Commun.* **11**, 5688 (2020).
- [32] C. Liu, C. Chen, X. Liu, Z. Wang, Y. Liu, S. Ye, Z. Wang, J. Hu and J. Wang, *Sci. Adv.* **6**, eaax7574 (2020).
- [33] Z. Wang, J. O. Rodriguez, L. Jiao, S. Howard, M. Graham, G. D. Gu, T. L. Hughes, D. K. Morr, V. Madhavan, *Science* **367**, 104 (2020).
- [34] P. Fulde and R. A. Ferrell, *Phys. Rev.* **135**, A550 (1964).
- [35] A. I. Larkin, and Y. N. Ovchinnikov, *Zh. Eksp. Teor. Fiz.* **47**, 1136–1146 (1964).
- [36] Private communication.
- [37] F. Ma, W. Ji, J. Hu, Z.-Y. Lu, and T. Xiang, *Phys. Rev. Lett.* **102**, 177003 (2009).
- [38] K. Liu, Z.-Y. Lu, and T. Xiang, *Phys. Rev. B* **93**, 205154 (2016).
- [39] J. K. Glasbrenner, I. I. Mazin, Harald O. Jeschke, P. J. Hirschfeld, Roser Valentí, *Nat. Phys.* **11**, 953 (2015).
- [40] P. Chandra, P. Coleman and A. I. Larkin, *Phys. Rev. Lett.* **64**, 88 (1990).
- [41] J. Hu, B. Xu, W. Liu, N. Hao, Y. Wang, *Phys. Rev. B* **85**, 144403 (2012).
- [42] D. Wang, L. Kong, P. Fan, H. Chen, S. Zhu, W. Liu, L. Cao, Y. Sun, S. Du, J. Schneeloch, R. Zhong, G. Gu, L. Fu, H. Ding, H.-J. Gao, *Science* **362**, 333 (2018).
- [43] A. Buzdin, *Phys. Rev. Lett.* **101**, 107005 (2008).
- [44] L. Fu, *Phys. Rev. Lett.* **104**, 056402 (2010).
- [45] S. Vijay and L. Fu, *Phys. Rev. B* **94**, 235446 (2016).
- [46] J. Alicea, Y. Oreg, G. Refael, F. von Oppen, M. P. A. Fisher, *Nat. Phys.* **7**, 412 (2011).
- [47] P. Bonderson, M. Freedman, C. Nayak, *Phys. Rev. Lett.* **101**, 010501 (2008).
- [48] T. Karzig, C. Knapp, R. M. Lutchyn, P. Bonderson, M. B. Hastings, C. Nayak, J. Alicea, K. Flensberg, S. Plugge, Y. Oreg, C. M. Marcus, and M. H. Freedman, *Phys. Rev. B* **95**, 235305 (2017).
- [49] R. AguadoLa, *Rivista del Nuovo Cimento* **40**, 523 (2017).
- [50] R. AguadoLa, and L. P. Kouwenhoven, *Physics Today* **73**, 44 (2020).
- [51] S.-B. Zhang, A. Calzona, and B. Trauzettel, *Phys. Rev. B* **102**, 100503(R) (2020).
- [52] S.-B. Zhang, W. B. Rui, A. Calzona, S.-J. Choi, A. P. Schnyder, and B. Trauzettel, *Phys. Rev. Research* **2**, 043025 (2020).

## FIRST-PRINCIPLES CALCULATING METHODS

Our first-principles crystal-structure calculations are performed within the density functional theory framework using the Vienna ab initio simulation package (VASP) [1, 2]. The approach relies on all-electron projector augmented-wave (PAW) [3] basis set combined with the generated gradient approximation (GGA) with the exchange-correlation functional of Perdew, Burke, and Ernzerhof (PBE) [4]. The cutoff energy for the plane-wave expansion was set to 400 eV and a k-point mesh of  $2 \times 12 \times 1$  was used in the dynamic-relaxation calculation. Within the domain wall, due to the breaking of Fe-Se/Te bonds, d-orbit electrons of Fe atoms become more localized, which may induce a Hubbard U effect. To take this condition into account, we apply a Hubbard U interaction onto the Fe atoms within the DW. The Hubbard values vary from 0 to 2 eV.

For the Fe(Te, Se) super cell shown in Fig. 1 in the main text, we calculate the density of states shown in Fig. 4 (a). We also simulate the STM images with different energy shown in Fig. 4 (b) and (c). As shown in Fig. 4 (a). One can find that the states from iron are dominated and those from Se, Te is very small near 0eV, while the states from Se, Te become sizable with deep energy such as 3eV. As a result, the contrast of the simulated the STM image is light with energy near 0eV and the contrast of the simulated the STM image is high with energy near -3eV. Note that details of atom patterns in Fig. 4 (b) and (c) are same, the only difference is the contrast. Hence, we show the figure with high contrast in Fig. 1 in the main text without inducing the confusion.

To estimate the strength of the effective Zeeman field in the DW, we start from the Heisenberg magnetic exchange model

$$H_m = -J \sum_{i < j} \vec{S}_i \cdot \vec{S}_j, \quad (6)$$

where  $\langle i, j \rangle$  denotes the nearest-neighbor site. Due to the bugle structure, Fe-Fe distance in the DW is smaller than the outside thus every Fe atom has four nearest neighbor. So the energy difference between FM and AFM can be derived as  $\Delta E = H_{AFM} - H_{FM} = 8J|\langle S_i^y \rangle|^2$ . Substituting it into the definition of  $h_y$ , we can obtain

$$h_y = \frac{n\mu_B \Delta E}{8\langle S_i^y \rangle}. \quad (7)$$

From the results of our first-principles calculation, the parameters can be obtained as  $n = 2$ ,  $\langle S_i^y \rangle = 1.75\mu_B$ ,  $\Delta E = 385\text{meV}$ , which gives  $h_y = 55\text{meV}$ . The width of DW is  $6.2 \text{ \AA}$  and the Fermi velocity is  $v_F = 216 \text{ meV\AA}$ , then the phase shift caused by the DW is  $\Delta\phi = \frac{2h_y L}{v_F} = 3.16 \sim \pi$ . As shown in Fig. 5(a) and (b), we also calculate the lattice pattern with domain walls involving two lines of irons, similarly every 1D iron chain tends to form a FM order, however the two FM iron chains can couple as collinear FM or AFM. Corresponding, the DW observed by STM is larger, which is shown in Fig. 5(c). By tuning the distance between two iron chains, we find its magnetic configuration is determined by the distance  $d$ . As shown in Fig. 5(d), when the distance decrease from  $2.60\text{\AA}$  to  $2.30 \text{ \AA}$ , the two iron chains transform from collinear AFM to FM order, which makes the DW possess a net effective Zeeman field. Back to the real condition, due to the breaking of chemical bonds in the DW there exists a compressive stress to force two iron chains get closer, which makes the DW get spontaneous magnetization.

## DERIVATION OF ANDREEV BOUND STATE

As shown in Fig. 6(a), Andreev reflection happens at the interface of S/F, which generates left- and right-moving holes in the F region. However, in the left (right) S region, only right-moving (left-moving) electrons and holes have contribution to the bound state. To obtain the wave functions in different regions, we can first put a four-component trivial solution

$$\psi = \psi_\lambda e^{\lambda x} e^{ik_y y} \quad (8)$$

into the DBdG equation ( $\varepsilon$  is the eigenvalue of energy)

$$H_{BdG}(k_x \rightarrow -i\partial_x, k_y)\psi = \varepsilon\psi, \quad (9)$$

we get the secular equation

$$\det|H_{BdG}(-i\lambda, k_y) - \varepsilon| = 0 \quad (10)$$

In the FM region, the wave number  $\lambda$  is obtained as

$$\lambda_{\alpha\beta} = i\alpha \frac{h_y + \beta \sqrt{(\varepsilon - \alpha\mu)^2 - v^2 k_y^2}}{v}$$

where  $\alpha = \pm 1$ ,  $\beta = \pm 1$ . Substituting  $\lambda_{\alpha\beta}$  into its corresponding eigenvectors, we get the trivial solutions in FM region as

$$\psi_1^F = \frac{1}{\sqrt{2}} \begin{pmatrix} 0 \\ 0 \\ e^{i\alpha} \\ 1 \end{pmatrix} e^{ik_h - x}, \psi_2^F = \frac{1}{\sqrt{2}} \begin{pmatrix} 0 \\ 0 \\ -e^{-i\alpha} \\ 1 \end{pmatrix} e^{ik_h + x},$$

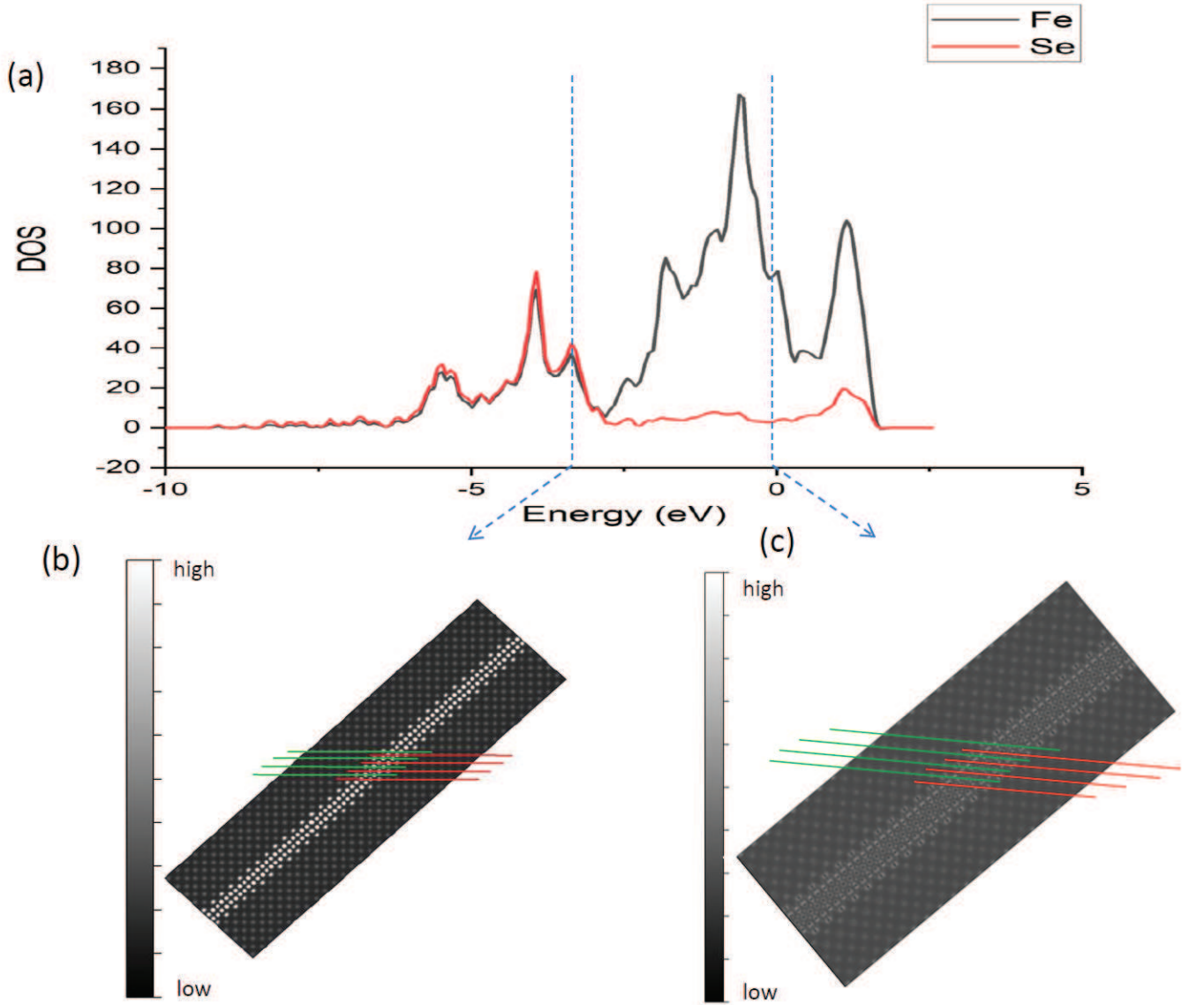


FIG. 4: (a) The density of states of the Fe(Te,Se) super cell shown in Fig. 1 in the main text. (b) and (c) The (Te, Se) charge density patterns with energy of about -3eV and 0eV, respectively. These patterns can simulate the STM images.

$$\psi_3^F = \frac{1}{\sqrt{2}} \begin{pmatrix} e^{-i\alpha'} \\ 1 \\ 0 \\ 0 \end{pmatrix} e^{ik_e - x}, \quad \psi_4^F = \frac{1}{\sqrt{2}} \begin{pmatrix} -e^{i\alpha'} \\ 1 \\ 0 \\ 0 \end{pmatrix} e^{ik_e + x},$$

where  $k_{h\pm} = \frac{h_y \pm \sqrt{(\varepsilon - \mu)^2 - v^2 k_y^2}}{v}$ ,  $k_{e\pm} = \frac{-h_y \pm \sqrt{(\varepsilon + \mu)^2 - v^2 k_y^2}}{v}$ ,  $e^{i\alpha} = \frac{vk_y + i\sqrt{(\varepsilon - \mu)^2 - v^2 k_y^2}}{\sqrt{(\varepsilon - \mu)^2}}$ ,  $e^{i\alpha'} = \frac{vk_y + i\sqrt{(\varepsilon + \mu)^2 - v^2 k_y^2}}{\sqrt{(\varepsilon + \mu)^2}}$ . The wave functions in FM region should be the linear combination of above four eigenvectors

$$\Psi_M = \sum_{i=1}^4 c_i \psi_i^F, \quad (11)$$

which contains left- and right-moving electrons, and left- and right-moving holes which are generated from Andreev reflecting. As shown in Fig. 6, in the left (right) superconducting region, the corresponding Andreev bound states are the left-moving (right-moving) electron and hole which are transmitted from the FM region and should exponential



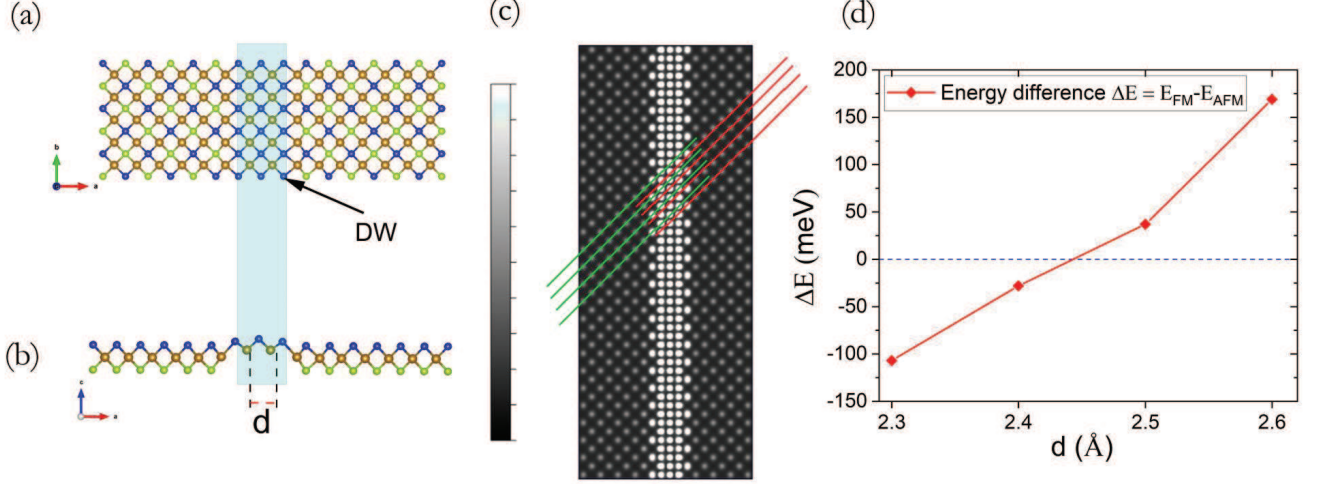


FIG. 5: (a) Top and (b) side view of two-iron-chains DW structure (c) Simulated STM image for two-iron-chains DW. (d) Energy difference between FM and collinear AFM of two iron chains varies with its distance

decay away. Thus the wave function in left (right) superconducting region is given as

$$\psi_1^l = \frac{1}{2} \begin{pmatrix} -e^{-i\gamma} \\ -e^{-i\gamma} e^{i\beta} \\ e^{i\beta} e^{-i\frac{\varphi}{2}} \\ e^{-i\frac{\varphi}{2}} \end{pmatrix} e^{ik_l - x}, \psi_2^l = \frac{1}{2} \begin{pmatrix} -e^{i\gamma} \\ -e^{i\gamma} e^{i\beta} \\ e^{i\beta} e^{-i\frac{\varphi}{2}} \\ e^{-i\frac{\varphi}{2}} \end{pmatrix} e^{ik_l + x},$$

where  $\gamma = \arccos \frac{\varepsilon}{\Delta_0}$ ,  $e^{i\beta} = \frac{vk_y + i\sqrt{(\mu - \Omega)^2 - v^2 k_y^2}}{\sqrt{(\mu - \Omega)^2}}$ ,  $k_{l\pm} = -\frac{\sqrt{(\mu \pm \Omega)^2 - v^2 k_y^2}}{v}$  with  $\Omega = \sqrt{\varepsilon^2 - \Delta_0^2}$ . And

$$\psi_1^r = \frac{1}{2} \begin{pmatrix} -e^{i\gamma} \\ -e^{i\gamma} e^{-i\beta} \\ e^{-i\beta} e^{i\frac{\varphi}{2}} \\ e^{i\frac{\varphi}{2}} \end{pmatrix} e^{ik_r - x}, \psi_2^r = \frac{1}{2} \begin{pmatrix} -e^{-i\gamma} \\ -e^{-i\gamma} e^{i\beta} \\ e^{i\beta} e^{i\frac{\varphi}{2}} \\ e^{i\frac{\varphi}{2}} \end{pmatrix} e^{ik_r + x},$$

where  $k_{r\pm} = \frac{\sqrt{(\mu \pm \Omega)^2 - v^2 k_y^2}}{v}$ . Similarly, the wave function in left (right) superconducting region can be expressed as

$$\Psi_{L/R} = \sum_{\gamma=1,2} t_{\gamma}^{l/r} \psi_{\gamma}^{l/r}. \quad (12)$$

Note that the energy scope we are interested in is  $\varepsilon < \Delta_0$ . Now we consider two limitations about chemical potential  $\mu$ . First, for  $\mu \rightarrow 0$ , the momentum along the DW is independent of the chemical potential and the wave functions of Andreev bound state decay in the superconducting region rapidly without propagation. The wave function of electrons in the left superconducting region can be simplified as

$$\frac{1}{\sqrt{1 + (\frac{\varepsilon}{\Delta_0})^2}} \left( -\frac{\varepsilon}{\Delta_0}, -\frac{v_F k_y + i\sqrt{\varepsilon^2 - v_F^2 k_y^2 - \Delta_0^2}}{\Delta_0}, 0, 1 \right)^T e^{i(-\frac{\sqrt{\varepsilon^2 - v_F^2 k_y^2 - \Delta_0^2}}{v_F})x}.$$

The other wave functions can be obtained in the same way. Secondly, for  $\mu \gg \Delta_0$ , it is reasonable to introduce the Fermi wave vector as  $k_F = \frac{\mu}{v_F}$  and  $k_y = k_F \sin \theta$ , where  $\theta$  is the incident angel. Under this approximation, the wave

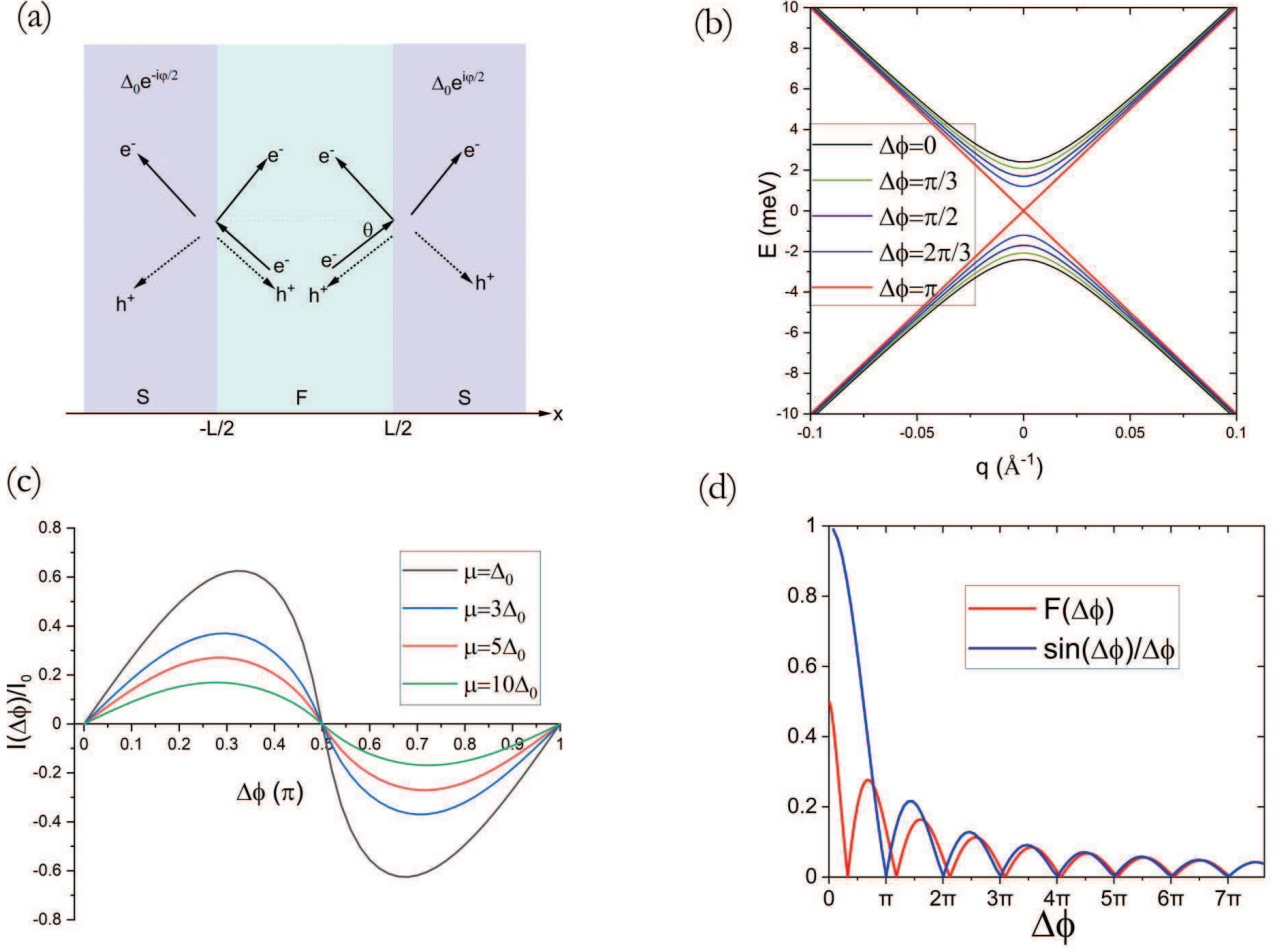


FIG. 6: (a) Andreev reflection in the S/F/S junction. (b) Energy dispersion of Andreev bound state. (c) Current in the phase battery varies with the phase shift and chemical potential. (d) Critical Josephson current in S/F/S junction and its approaching function.

number in superconducting region can be divided into real and imaginary part which represents the phase oscillation and amplitude decay respectively, here we give an example for right-moving hole in superconducting region, which is

$$k_{r+} = \frac{\sqrt{\varepsilon^2 - \Delta_0^2}}{\sqrt{\varepsilon^2 - \Delta_0^2 - \mu^2 \sin^2 \theta}} k_F + i \frac{\sqrt{\Delta_0^2 + \mu^2 \sin^2 \theta - \varepsilon^2}}{v}$$

and the corresponding eigenvector is

$$\frac{1}{2} \left( -\frac{\varepsilon + \sqrt{\varepsilon^2 - \Delta_0^2}}{\Delta_0}, \frac{i(\varepsilon + \sqrt{\varepsilon^2 - \Delta_0^2})}{\Delta_0}, i, 1 \right)^T$$

In the FM region, reasonably we set  $\mu = 0$  because such a large Fermi vector mismatch effectively accounts for a barrier between the nonsuperconducting and superconducting regions of the surface of the topological insulator, which is expected to be present experimentally [5]. Now we consider the boundary condition at the domain wall, the continuity of wave functions requests

$$\Psi_M|_{x=\frac{L}{2}} = \Psi_R|_{x=\frac{L}{2}} \quad (13)$$

$$\Psi_M|_{x=-\frac{L}{2}} = \Psi_L|_{x=-\frac{L}{2}}. \quad (14)$$

Eq. (8) and (9) gives a determinant of coefficients  $c_i$  ( $i = 1, 2, 3, 4$ ) and  $t_\gamma^{l/r}$  ( $\gamma = 1, 2$ ). The determinant, namely  $\mathcal{M}$ , is a  $8 \times 8$  matrix, which can be derived as:

$$\mathcal{M} = \begin{pmatrix} \psi_1^F|_{x=\frac{L}{2}} & \psi_2^F|_{x=\frac{L}{2}} & \psi_3^F|_{x=\frac{L}{2}} & \psi_4^F|_{x=\frac{L}{2}} & 0 & 0 & \psi_1^r|_{x=\frac{L}{2}} & \psi_2^r|_{x=\frac{L}{2}} \\ \psi_1^F|_{x=-\frac{L}{2}} & \psi_2^F|_{x=-\frac{L}{2}} & \psi_3^F|_{x=-\frac{L}{2}} & \psi_4^F|_{x=-\frac{L}{2}} & \psi_1^l|_{x=-\frac{L}{2}} & \psi_2^l|_{x=-\frac{L}{2}} & 0 & 0 \end{pmatrix}. \quad (15)$$

The nontrivial solution of the wave function of the S/F/S system asks for

$$\text{Det } \mathcal{M} = 0, \quad (16)$$

that gives the same expression of energy spectrum for both  $\mu \rightarrow 0$  and  $\mu \gg \Delta_0$

$$\varepsilon = \sqrt{v_F^2 k_y^2 + \Delta_0^2 \cos^2\left(\frac{\varphi - \Delta\phi}{2}\right)}.$$

Here,  $\Delta\phi = \frac{2h_y L}{v_F}$ . For  $\mu \rightarrow 0$ , we have  $k_y \rightarrow 0$ . For  $\mu \gg \Delta_0$ , we have  $k_y = \frac{\mu}{v_F} \sin \theta$  with  $k_y \rightarrow 0$  for  $\theta \rightarrow 0$ , i.e., a small incident angle with small momentum. The dispersion spectrum is shown in Fig. 6(b), with  $\varphi = 0$ , the phase shift  $\Delta\phi$  determines the gap, only when  $\Delta\phi = \pi$  the bound state is gapless. Fig. 6(c) shows how the current varies with the phase-shift and chemical potential in the phase battery. When the scattering effect is considered in the real junction, the critical current of a S/F/S junction has the form [6, 7]

$$I(\varphi, \Delta\phi) = \frac{\pi \Delta_0^2}{4e R_N T} F(\Delta\phi) \sin \varphi \quad (17)$$

where  $F(\Delta\phi) = (\Delta\phi)^2 \int_{\Delta\phi}^{\infty} \frac{\cos x}{x^3} dx$ . When  $\Delta\phi \gg 1$  the critical current is simplified as

$$I_c = \frac{\pi \Delta_0^2}{4e R_N T} \frac{\sin \Delta\phi}{\Delta\phi}.$$

Here, this derivation requests a clean limit, which is  $\tau h_y \gg 1$ . Note that backscattering is forbidden due to the special spin-momentum locking, which gives a large relaxation time  $\tau$ , this critical current relationship is suitable in our TI-based S/F/S system. As is shown in Fig. 6(d), when  $\Delta\phi \gg 1$ , the critical current turns to be zero at  $\Delta\phi = n\pi$ , correspondingly a gapless subgap state occurs. Thus the vanish of critical current could be a signal of the emergence of nontrivial gapless topological superconducting state.

### MAJORANA ZERO-ENERGY MODEL

It is useful to construct a low energy theory to describe the subgap state. For  $\mu \gg \Delta_0$ ,  $\theta \rightarrow 0$ , we have  $k_y \rightarrow q \sim 0$ , and  $\varphi = 0$ , the eigen-wave functions can be simplified as

$$\begin{aligned} \xi_1 &= \frac{1}{2}(-e^{i\frac{\Delta\phi}{2}}, ie^{i\frac{\Delta\phi}{2}}, i, 1)^T e^{ik_F x - \frac{x}{\xi_0}} \\ \xi_2 &= \frac{1}{2}(-e^{-i\frac{\Delta\phi}{2}}, -ie^{-i\frac{\Delta\phi}{2}}, -i, 1)^T e^{-ik_F x - \frac{x}{\xi_0}}, \end{aligned}$$

where  $\xi_0 = \frac{v_F}{\Delta_0}$ . Using  $\xi_1$  and  $\xi_2$  as basis, we can project  $H_{BdG}$  onto the subspace as  $h_{ij} = \langle \xi_i | H_{BdG} | \xi_j \rangle$ . Then the low-energy effective Hamiltonian of the subgap state can be obtained as

$$H_{eff} = \tilde{v} k_y \sigma_y - \Delta_0 \cos \frac{\Delta\phi}{2} \sigma_z \quad (18)$$

where  $\tilde{v} = v_F [\cos k_F L + (\frac{\Delta_0}{\mu}) \sin k_F L] \Delta_0^2 / (\mu^2 + \Delta_0^2)$ . Note that at another limitation  $\mu \rightarrow 0$ , the low-energy effective Hamiltonian has the same form except that  $\tilde{v} = (1 + \frac{L}{\xi_0}) v_F \sim v_F$ . If there exists a boundary at  $y = 0$  makes the length of the FM region varies in  $y > 0$  and  $y < 0$ . More precisely, the phase shift caused by the effective Zeeman field has the distribution as

$$\Delta\phi(y) = \begin{cases} \pi + \epsilon, & y > 0 \\ \pi - \epsilon, & y < 0 \end{cases}. \quad (19)$$

Under this condition,  $\cos \frac{\Delta\phi}{2}$  has a sign change crossing the boundary. In fact, Eq. (11) is exact a 1D Dirac equation, where  $\Delta_0 \cos \frac{\Delta\phi}{2}$  acts as the mass term. The negative- and positive- mass boundary condition requests the Jackiw-Rebbi solution. The eigenenergy of the bound state is  $E = 0$  and the wave function is

$$\phi_{\pm}(y) = \frac{1}{\sqrt{2}} \begin{pmatrix} 1 \\ \pm i \end{pmatrix} e^{-y/\tilde{\xi}} \quad (20)$$

where  $\tilde{\xi}_0 = \frac{\tilde{v}}{\epsilon\Delta_0}$ .

---

\* Electronic address: haon@hmfl.ac.cn

- [1] G. Kresse and J. Furthmüller, Phys. Rev. B **54**, 11169 (1996).
  - [2] G. Kresse and D. Joubert, Phys. Rev. B **59**, 1758 (1999).
  - [3] P. E. Blchl, Phys. Rev. B **50**, 17953 (1994).
  - [4] J. P. Perdew, K. Burke, and M. Ernzerhof, Phys. Rev. Lett. **77**, 3865 (1996).
  - [5] Jacob Linder, Yukio Tanaka, Takehito Yokoyama, Asle Sudbo, and Naoto Nagaosa, Phys. Rev. B **81**, 184525 (2010).
  - [6] Buzdin A, Bulaevskii L.N, Panyukov S, Pis'Ma Zh. Eksp. Teor. Fiz **35**. 147-148 (1982).
  - [7] A. I. Buzdin, Rev. Mod. Phys. **77**, 935 (2005).
-